

A study of the physical properties of an active asteroid (6478 Gault)

Zhong-Yi LIN ^{1,*} Yu-Li CHENG,² Jean-Baptiste VINCENT,³
Xi-Liang ZHANG,^{4,5} Wing Huen Ip,¹ and Hsin-Chang CHI²

¹Institute of Astronomy, National Central University, Taoyuan, 32001, Taiwan

²Department of Physics, National Dong Hwa University, No. 1, Sec. 2, Da Hsueh Rd. Shoufeng, Hualien 97401, Taiwan

³DLR Institute of Planetary Research, Berlin, Germany

⁴Yunnan Observatories (YNAO), Chinese Academy of Sciences, Kunming 650216, China

⁵Key Laboratory of the Structure and Evolution of Celestial Objects, Chinese Academy of Sciences, Kunming 650216, China

*Email: zylin@gm.astro.ncu.edu.tw

Received 2020 April 29; Accepted 2020 June 30

Abstract

In 2019 January, the appearance of asteroid 6478 Gault immediately attracted attention because this object exhibited a long and thin tail that was quite different from the usual asteroids. This unexpected morphology placed asteroid 6478 Gault into the catalogue of active asteroids. We acquired photometric and spectroscopic observations on 37 nights from 2019 January to April using several telescopes, including LOT (1 m telescope) and SLT (40 cm telescope) at Lulin Observatory, and the 2.4 m telescope at Lijiang station of Yunnan Observatory. We did not find any reliable value for the rotational period of Gault during 2.5 hr and 5 hr observations on 2019 January 26 at Lijiang station and March 25 at Lulin Observatory, respectively. We classified 6478 Gault as a Q-type asteroid using visible spectrum and photometric measurements, including colors ($B - V_{\text{avg}} = 0.764 \pm 0.045$, $V - R_{\text{avg}} = 0.450 \pm 0.023$), and relative reflectance. By using Finson–Probstein analysis, the grain size for Gault’s tail 2 is larger than $20 \mu\text{m}$.

Key words: minor planets, asteroids: general — minor planets, asteroids: individual (6478 Gault)

1 Introduction

Discovered in 1988, 6478 Gault (formerly 1998 JC1, and simply “Gault” hereafter), with the orbital elements $e = 0.194$, $a = 2.305$ au, $i = 22^\circ.8$, is a main-belt asteroid. Gault has an absolute magnitude of 16.11 in the V band (Ferrín et al. 2019) and a diameter ranging from 2 km to 4 km depending on the assumption of a geometric albedo of 0.2 (for S-type) or 0.04 (for C-type). It was an unremarkable object until late 2018, when the Hawaii ATLAS survey first noticed that it had suddenly brightened and developed a

tail (Tonry et al. 2018). This made it a rare member of the class of active asteroids which is intermediate between asteroids and comets. These active asteroids have asteroid-like semi-major axes and Tisserand parameters ($TJ > 3.0$), but they can also exhibit comet-like mass loss, manifested optically as resolved comae and tails (Jewitt 2015). Until early 2020, about two dozen known active asteroids have been found, and some have been observed to repeat their activity during multiple orbit passages: 133P/Elst–Pizarro (Elst et al. 1996; Hsieh et al. 2004), 238P/Read (Hsieh et al. 2009,

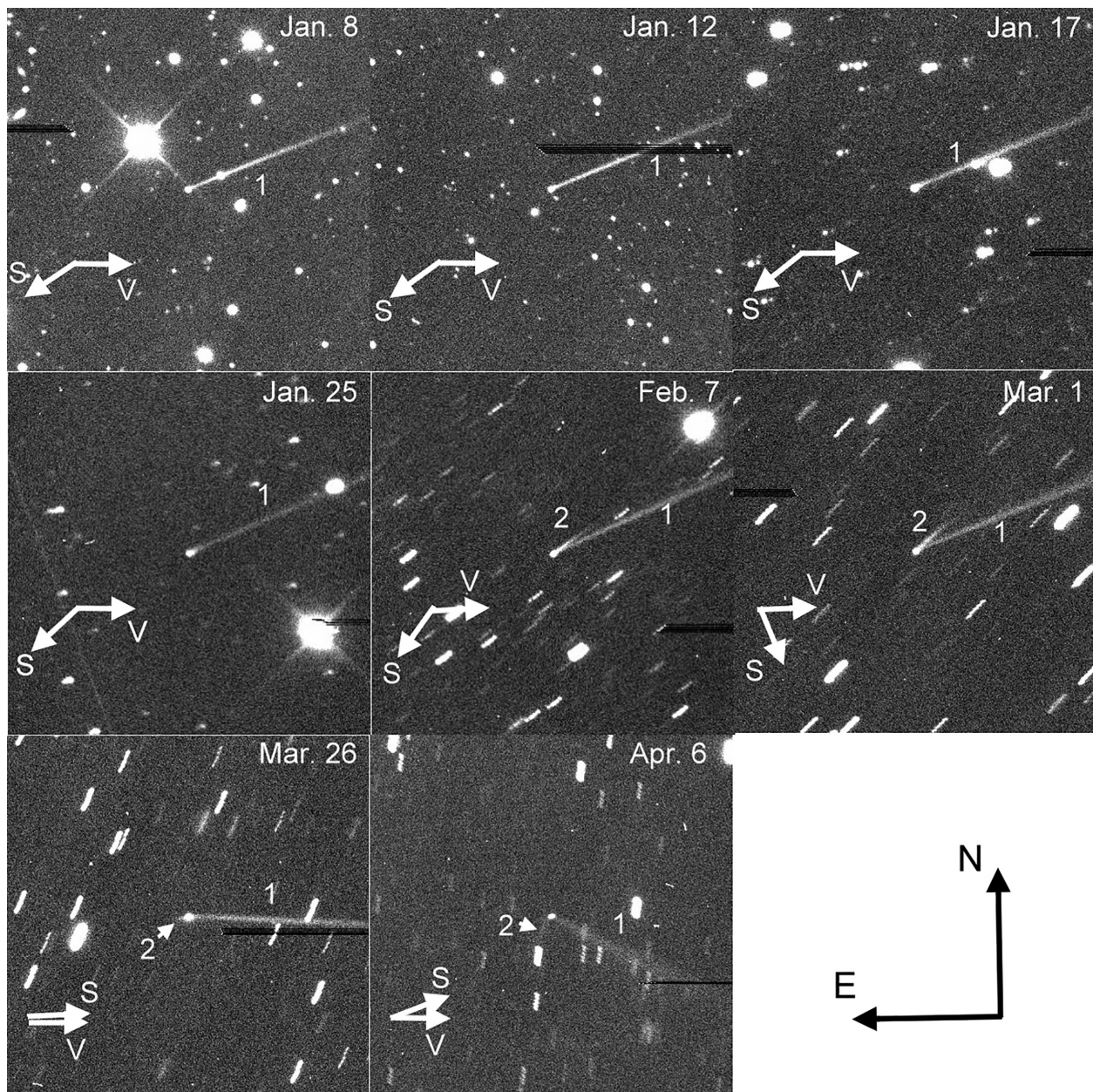


Fig. 1. Monitoring images of the evolution of the 6478 Gault dust tail by SLT of Lulin Observatory from 2019 January to April. The field of view is about $2'.6$ and the arrows indicate the solar direction (S) and the negative of Gault's velocity (V). The tails are identified with numbers (1, 2, and 3) in order of discovery.

2011, 2018b), 288P (Hsieh et al. 2012b, 2018b; Agarwal et al. 2016), 259P/Garradd (Jewitt et al. 2009; Hsieh & Chavez 2017), 313P/Gibbs (Hsieh et al. 2015; Hui & Jewitt 2015), 324P/La Sagra (Hsieh et al. 2012a; Hsieh & Shepard 2015), and 358P/PANSTARRS (Hsieh et al. 2018b). Several mechanisms have been proposed to explain such transient phenomena, including rotational breakup (e.g., 311P/PanSTARRS, Jewitt et al. 2013), asteroid impact (e.g., 596 Schelia; Bodewits et al. 2011; Moreno et al. 2011) and sublimation of subsurface ice in main belt comets (e.g., 133P/Elst–Pizarro; Hsieh et al. 2010). Studying each active asteroid to understand its mechanism of activity is therefore

necessary because it can provide clues to solar system phenomena such as primordial volatiles from MBC sublimation and material composition from rotation and impacts (Kleyna et al. 2019).

Monitoring images of Gault exhibiting its long, thin tail are shown in figure 1. A debris tail from Gault was first spotted on 2019 January 5 (Smith et al. 2019). The tail also turned up in archival data in 2018 December from the ATLAS and Pan-STARRS telescopes in Hawaii. In mid-January, a second, shorter, tail was detected by the Canada–France–Hawaii Telescope in Hawaii and the Isaac Newton Telescope in Spain, as well as by other observers (Hale

et al. 2019a, 2019b; Jehin et al. 2019; Lee 2019a; Ye et al. 2019b). The third one was detected by the NOT telescope after Earth passed through the projected orbital plane of Gault in early 2019 April (Jewitt et al. 2019). An analysis of the first two tails suggested the sudden release of tens of millions of kilograms of dust between 2018 October 28 and December 30 (Hui et al. 2019; Jewitt et al. 2019; Moreno et al. 2019; Ye et al. 2019a). The very low velocity of the ejected dust grains (Hui et al. 2019; Jewitt et al. 2019; Kleyna et al. 2019; Moreno et al. 2019; Ye et al. 2019a) and the absence of detectable gas in visible spectra (Jewitt et al. 2019) imply that the activity was not driven by the sublimation effect. Interestingly, Kleyna et al. (2019) determined that Gault has a rotation period of about 2 hr from their photometric data obtained in early 2019 February. Note that their lightcurve might not be derived directly from the nucleus because of coma contamination. But, it is noteworthy that this value is close to the spin barrier of ~ 2.2 hr estimated for a rubble pile asteroid, meaning its internal strength is too weak to sustain a fast rotation (e.g., Pravec & Harris 2000). As the archival data back in 2013 revealed an earlier phase of dust activity (Chandler et al. 2019), these authors therefore ruled out a single-impact collision as the origin of the activity and suggested instead that the most likely scenario to explain the activity of this asteroid is breakup of the surface material or landslides resulting from a YORP-induced rotational disturbance (Chandler et al. 2019; Hui et al. 2019; Jewitt et al. 2019; Kleyna et al. 2019; Marsset et al. 2019; Moreno et al. 2019; Ye et al. 2019a).

Although Gault is dynamically linked to the 25 Phocaea collisional family of S-type classification, its spectral and compositional similarity with this family had not been fully investigated (Sanchez et al. 2019). For example, near-infrared spectroscopy revealed that Gault is a silicate-rich (Q- or S-type) object (Marsset et al. 2019), but broadband colors and some visible spectra revealed that this active asteroid is more similar to C-type asteroids than S-types (Ye et al. 2019a; Jewitt et al. 2019; Lee 2019b). The purpose of our work is to perform detailed time-series photometric measurements with spectroscopic data obtained from the Lulin and Lijiang Observatories to determine the rotation period and exact taxonomic class of Gault. In section 2 the observation and data reduction will be described. The results of the data analysis and discussions in rotation period and taxonomic identification will be given in section 3. In section 4, we constrain the grain size of Gault's tail using a Finson-Probstein analysis of the comprehensive dataset from 2019 January to April, and this is followed by a summary in section 5.

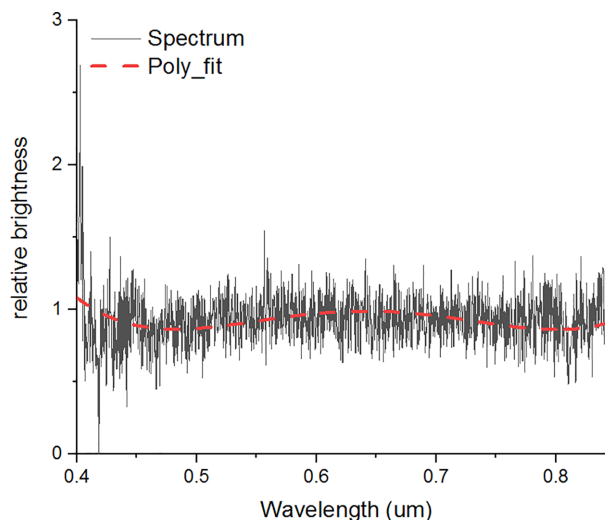


Fig. 2. A YFOSC spectrum of Gault obtained at the Lijiang 2.4 m telescope showing how it reflected light as a function of wavelength. To minimize the standard deviation of the errors, we smooth our asteroid spectrum by the polynomial curve shown with a dashed line. (Color online)

2 Observations

2.1 Spectrum and lightcurve

The optical spectrum of Gault was taken on 2019 March 15 using the Lijiang 2.4 m telescope at Lijiang station of Yunnan Observatories. The longitude, latitude, and altitude of the Lijiang station are $100^{\circ}01'48''$, $26^{\circ}42'42''$, and 3193 m, respectively. The Yunnan Faint Object Spectrograph and Camera (YFOSC) mounted on the Cassegrain telescope of 2.4 m aperture can quickly switch from photometry to spectroscopy. The detailed parameters of the telescope and YFOSC can be found in Wang et al. (2019). We used Grism 3, which provides a relatively low dispersion ($R \sim 2000$ at $600 \text{ nm pixel}^{-1}$) and wide wavelength coverage ($3400 \sim 9100 \text{ \AA}$). The resulting spectrum divided by a standard solar analog star (G5 IV, SA 102-1081) and normalized at 550 nm is shown in figure 2. To minimize the standard deviation of the errors for attempting taxonomic classification, we smoothed our data by curve fitting with polynomial functions. This was done using poly fitting from the IDL routine. The degree of the polynomial was selected to be four, such that the fit produces the smallest least squares fitting residuals. The obtained fitting curve is also shown as dashed lines in figure 2.

Time-series photometry with 1 min and 2 min cadences were also acquired with the Johnson-R filter in YFOSC on 2019 January 26 and in LOT on 2019 March 25. The field of view (FOV) of YFOSC is about $10'$, with a plate scale of $0''.57 \text{ pixel}^{-1}$. The time duration for the January 26 observation was about 2.5 hr, and the airmass varied between

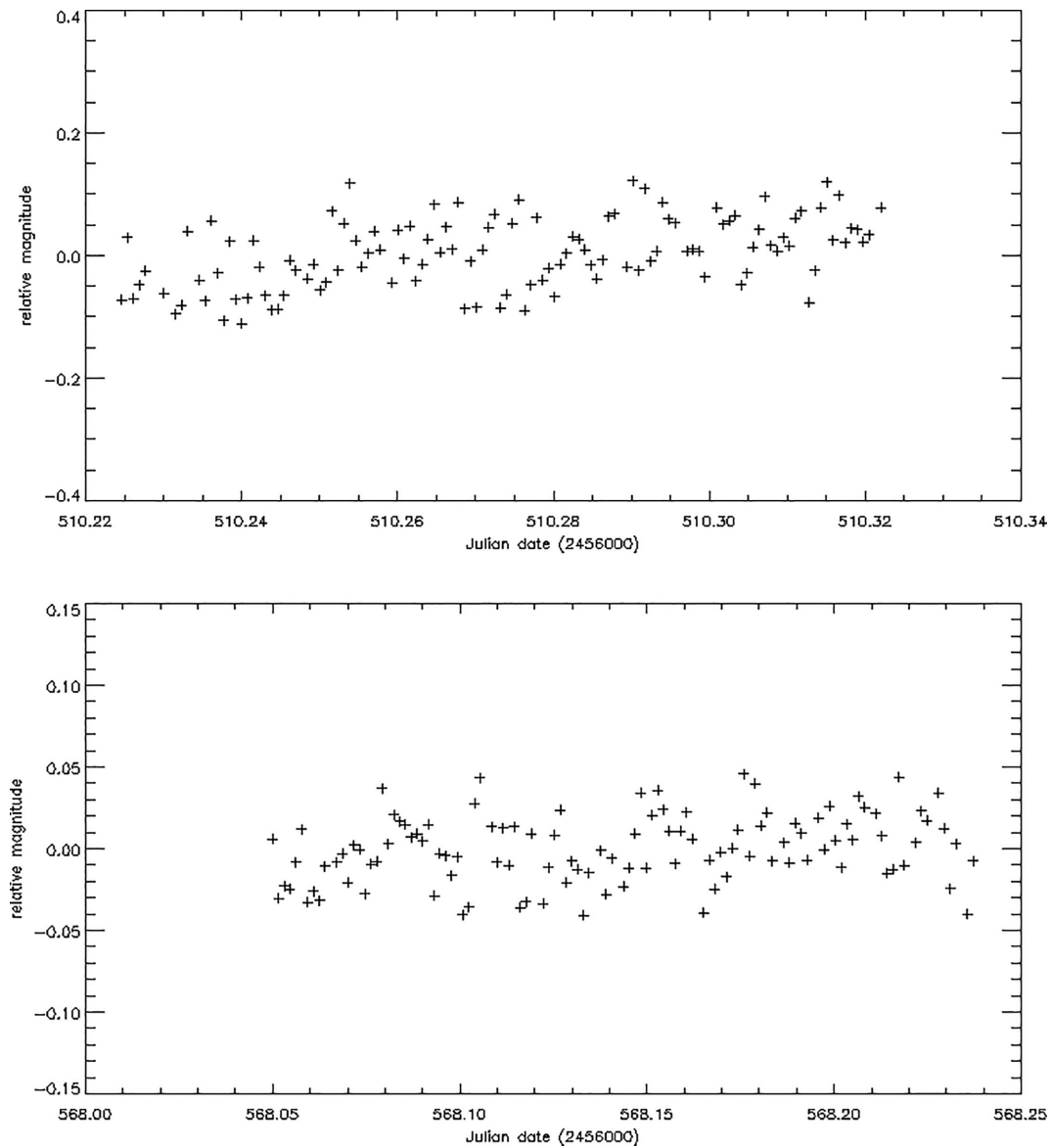


Fig. 3. Lightcurves of Gault obtained at Lijiang 2.4 m telescope (upper panel) on 2019 January 16 and the Lulin 1 m telescope (bottom panel) on 2019 March 25. The observational durations at the Lijiang and Lulin observatories were 2.5 hr and 5 hr, respectively. We cannot find the reliable rotational period as suggested by Kleyna et al. (2019).

1.29 and 1.67. The time span in the March observation was about 5 hr, and the images were acquired at a variety of airmasses from 1.10 to 2.11. Differential photometry using at least seven reference stars on all images was carried out by means of IDL routines based on DAOPHOT. For aperture photometry of both Gault and the reference stars, the mean value of the full-width half-maximum (FWHM) of the point spread functions of the reference stars in each image was used. In other words, the flux of the asteroid and those of the reference stars were computed using the same aperture size. The normalized lightcurves of Gault at Lijiang and Lulin observatories are shown in figure 3.

2.2 Imaging and colors

The photometric observations of Gault were made using the 1 m telescope (LOT) and the 16" Ritchey–Chrétien telescope (SLT) at the Lulin Observatory, Taiwan. The LOT with a FOV of 11' was installed in 2002 by the Institute of Astronomy, National Central University. The 2K × 2K charge-coupled device (CCD) camera, Sophia, manufactured by Apogee Instruments has a pixel scale of 0".39 pixel⁻¹. The SLT with a U42 CCD imaging camera was attached to the Cassegrain focus of the telescope. The focal length of the SLT was 2500 mm (with a 0.75× reducer), resulting in a 1 × 1 pixel-scale binning of 0".79 pixel⁻¹. The FOV of this system was

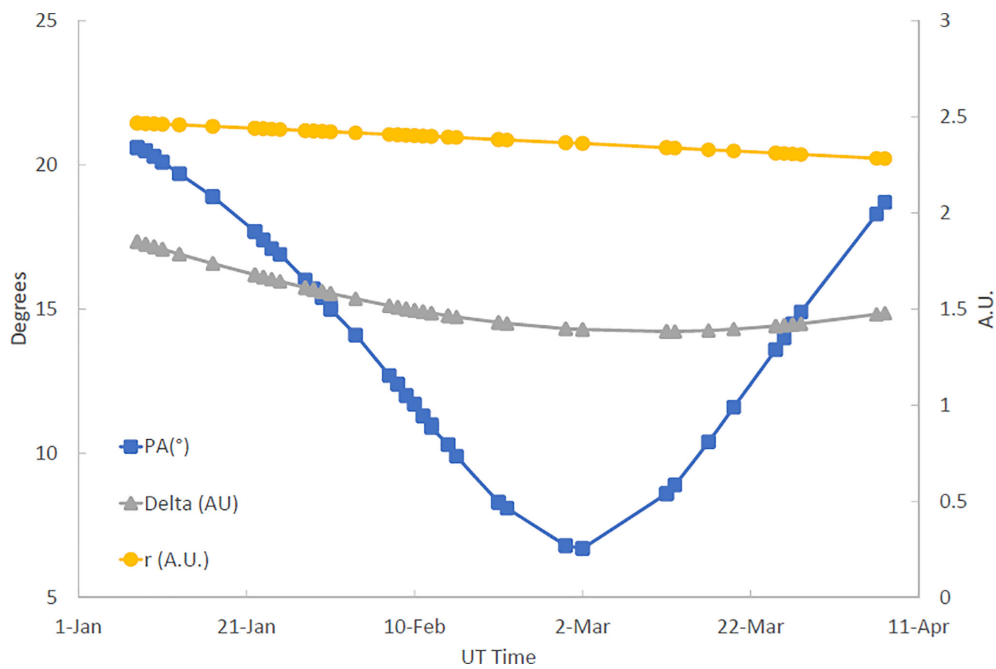


Fig. 4. Behavior of Δ (triangle), the distance from the observer to the object, r (circle), the distance from the sun to the object, and PA (square), the phase angle of the object. The symbols depict the UT dates when observations were acquired from Lulin Observatory. (Color online)

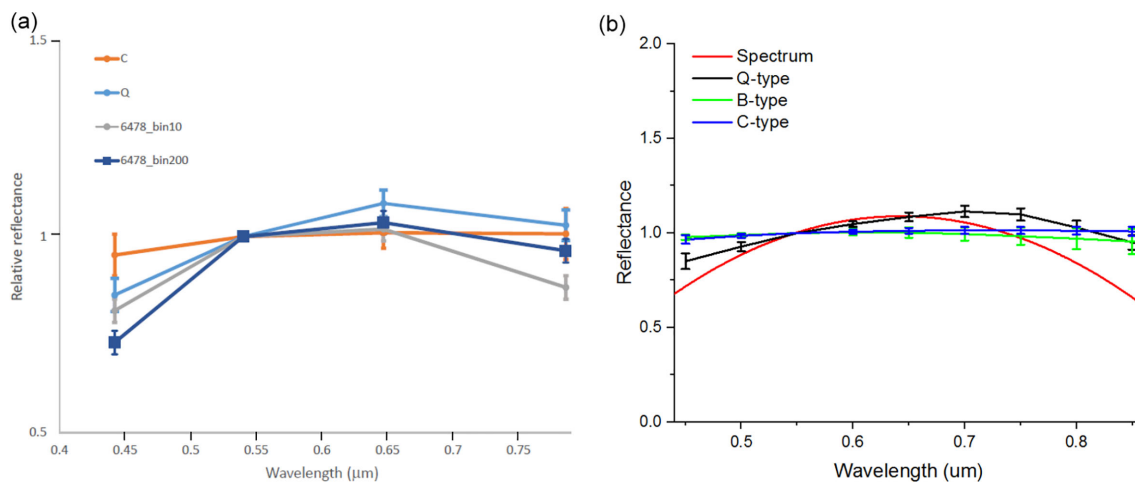


Fig. 5. Reflectance spectrum of 6478 Gault from Lijiang station normalized to $0.55\ \mu\text{m}$ in the range $0.45\text{--}0.9\ \mu\text{m}$. Left panel: the smoothed asteroid spectrum with a 1 nm (bin10) and 20 nm (bin200) boxcar average and comparison to that of the C- and Q-type asteroids (Bus-DeMeo taxonomy). We note that a better match in this smoothed spectrum between 6478 Gault and Q-type asteroids is to rely on R - and I filters. Right panel: the result of the M4AST online tool; the Gault spectrum after polynomial curve fitting is much closer to Q-type classification than the other two classes (B and C). (Color online)

$27' \times 27'$. At LOT, Gault was observed for 39 nights from 2019 January to April with B , V , R , and I Johnson filters centered at 0.45 , 0.55 , 0.67 , and $0.81\ \mu\text{m}$, respectively. At SLT, we mostly observed in the same time slot as LOT did through a Bessel R -filter with some additional B , V , and I images. The observational details of the color photometric measurements are shown as dots in figure 4. The asteroid phase angle and geocentric and heliocentric distances changed in the ranges $20^\circ.7$ to $17^\circ.4$,

1.85 to $1.38\ \text{au}$, and 2.47 to $2.28\ \text{au}$, respectively. The data reduction followed standard procedures, including bias and dark-frame subtraction and flat-field correction. The dark frames and the flat frames were taken at the beginning and the end of each observation night. To calibrate the resulting magnitudes and colors in LOT, a number of photometric standard fields selected from the list of Landolt (1992) were also observed during the photometric nights.

Table 1. M4AST results relative to the first three curve matches.*

Type	χ^2	Standard error	Mean squared error
Q	0.0026425	0.0482152	0.0022594
B	0.0027270	0.0546955	0.0026987
C	0.0036647	0.0628235	0.0035658

*Computed by normalizing the spectrum and the taxonomic type to their median values.

3 Results and discussion

3.1 Spectroscopic results

To assign a taxonomic type for the Gault spectra presented in this paper we used the Bus–DeMeo taxonomy (DeMeo et al. 2009). This taxonomy is based on principal component analysis of the VNIR spectra. We classified our spectra in this taxonomy using two methods: (i) by smoothing the spectrum comparing with reflectance values (see sub-subsection 3.2.2) computed from the Bus–DeMeo photometry, and (ii) by performing curve matching with the 25 classes defined by the taxonomy (using the M4AST website; Popescu et al. 2012). These two methods were used to determine how closely the asteroid spectra can be fitted by the standard spectrum of each class. The first method is to smooth the asteroid spectrum with the 1 nm and 20 nm boxcar average and then to compare this curve to the standard spectrum. The smoothed spectrum (figure 5a) shows a curved spectrum (within the limits of noise) in agreement with the Q-type classification indicated in the literature (a visible spectrum by Bus & Binzel 2002). The second one involves first fitting the spectrum with a polynomial curve and then comparing this curve to the standard spectrum at the wavelengths given in the taxonomy. In our approach to fitting, we decided to use the chi-square (χ^2) test for goodness of fit (Bevington & Robinson 1992). Table 1 displays the first three curve matches by the lowest standard deviation. After using the M4AST online tool, Gault can also be associated with Q-type asteroids (figure 5b). This taxonomic classification is consistent with the results from near-infrared spectra exhibiting deep absorption bands near 1 and 2 μm consistent with an S- or Q-type surface composition (Marsset et al. 2019; Sanchez et al. 2019) and from our visible photometric measurements (see sub-subsection 3.2.1). It is noteworthy that the other two possibilities (B- and C-class) have been reported by Lee (2019b) and Jewitt et al. (2019), the spectrum in short wavelengths is very noisy (figure 5), and the chi-square values in table 1 for those three classes are very close to each other if we take the errors into account. We therefore need photometric data (i.e., colors) to tell us whether Gault is S-complex or C-complex.

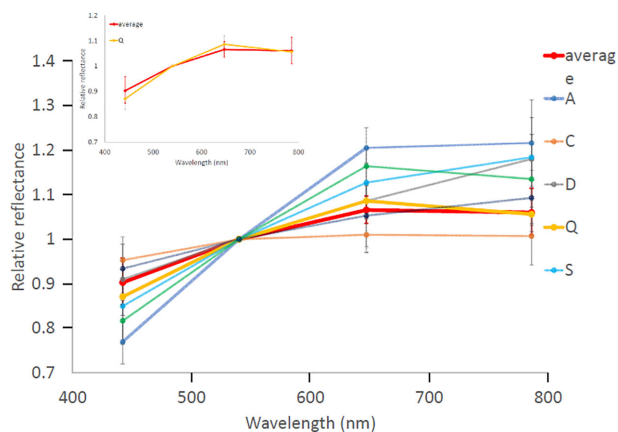


Fig. 6. The averaged and comparison-relative reflectance of Gault shows that the Q-type relative reflectance is the best fit (upper left panel). (Color online)

3.2 Photometric results

3.2.1 Spectral class and colors

The measurements of Gault at Lulin were carried out with *B*, *V*, *R*, and *I* filters with the aim of deriving its taxonomic type according to its surface colors. The Gault images using the sequence *R–B–R–V–R–I–R* were acquired to remove the effect of magnitude variation due to the asteroid’s rotation, but the effect of phase angle was not corrected because the change of phase angle is small ($\sim 3^\circ$), and the correction of phase reddening was not done here. By subtracting the standard solar colors ($B - V = 0.665$, $V - R = 0.367$, and $V - I = 0.705$; Howell 1995), we obtained the averaged relative reflectance of Gault in figure 6. The relative reflectance is normalized to 1 at 0.55 μm (*V*-band). Through comparing with the known relative reflectance (i.e., the Bus–DeMeo system), we classified Gault as a Q-type asteroid.

The colors of Gault are compared with those of other asteroid spectral types from Dandy, Fitzsimmons, and Collander-Brown (2003), and all the data points and averaged values are shown in figure 7. Gault is closer to S-complex. A silicate-rich object (S- or Q-type) is consistent with the result from the near-infrared spectrum (Marsset et al. 2019; Sanchez et al. 2019) and makes Gault a slight relative of the 25 Phocaea collisional family.

3.2.2 Rotational period

Kleyna et al. (2019) had an extensive series of observations but they found no convincing lightcurve, meaning the rotational period could only be estimated at ~ 1 hr for one peak, and ~ 2 hr for two peaks. Moreno et al. (2019) also did not get a rotational signature from their long series of observations acquired at the TRAPPIST North and South telescopes. Instead, Ferrín, Fornari, and Acosta (2019) found a rotational period of $P_{\text{rot}} = 3.360 \pm 0.005$ hr and showed

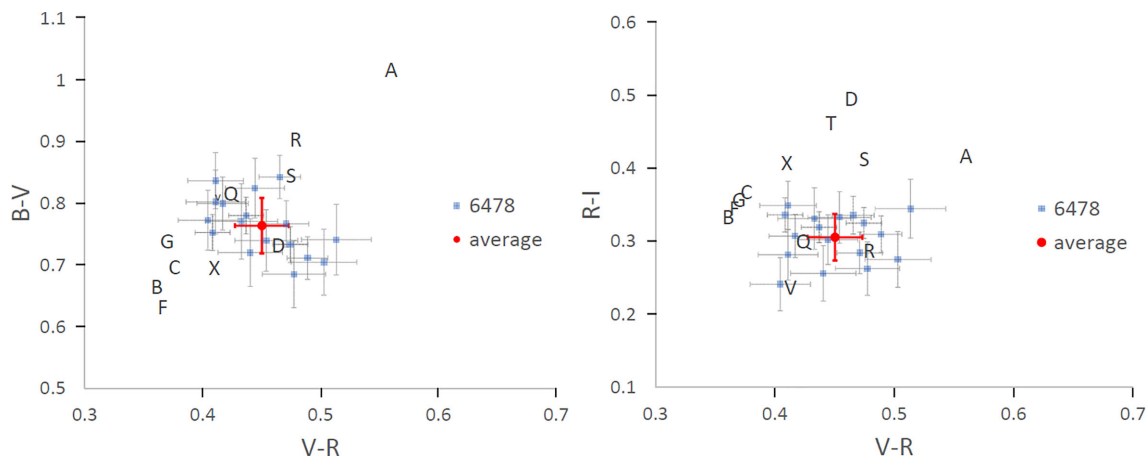


Fig. 7. Obtained asteroid Gault colors (marked with error bars) in color diagrams ($R - I$) vs. ($V - R$) in the left panel and ($B - V$) vs. ($V - R$) in the right panel. The blue dots are the data from 2019 January to April, and the red dot is the average value. (Color online)

evidence that 6478 might be a binary from their comprehensive dataset acquired on 41 nights from 2019 January to June. Jewitt et al. (2019) did not get any reliable period via their 3 hr observations. They claimed that the lack of a measurable lightcurve is consistent with Gault having a shape that is close to azimuthally symmetric, or a rotation vector parallel to the line of sight, or with the scattering cross-section being dominated by dust (Jewitt et al. 2019; Sanchez et al. 2019). Our photometric time-series data shown in figure 3 uses 5000 km ($\sim 6''.6$) as a measured radius on 2019 January 26 and March 25. Using the Lomb–Scargle method (Lomb 1976) to analyze these data, we did not find any reliable value for the rotational period of Gault. The same invariance of the photometry is observed using 10000 km ($\sim 13''.2$). In addition, we used 2 hr and 3.36 hr as the folding interval to represent the original lightcurve, but still could not get any meaningful values. Expect for the explanation made by Jewitt et al. (2019) and Sanchez et al. (2019), the non-repeating short-term variation in our dataset might possibly be caused by low-level cometary activity hiding the nucleus.

4 Tails

We report the detection of several dust tails in our dataset; their measured positions are given in table 2.

Tail 1 is the most prominent and can be observed in all images. It extends in the anti-velocity direction, with a lag of about 22° until the beginning of 2019 March. Afterwards, the tail direction migrates up to 29° ahead of the anti-velocity vector. This is due to the rapid change of observing geometry as the object reaches closest approach to Earth on March 11.

Tail 2 is only visible for a few weeks. We detected it for the first time on February 7, and it had almost completely faded away by April 6.

We interpret these tails as signatures of dust emission from the asteroid from at least two independent events. In order to constrain the timeline and physical properties of the dust grains present in those tails, we performed a Finson–Probstein analysis of the tail geometry (Finson & Probstein 1968). This model describes the motion of dust particles ejected from a cometary nucleus, accounting for solar gravity and radiation pressure. It leads to a geometric description of the dust environment, typically a grid of *synchrones* and *syndynes* which represent respectively the locations of particles released at the same time, or with the same size. Although simple, this model is commonly used in cometary science and leads to a robust description of the particles present in cometary tails, as well as good constraints on their time of emission. We use here the implementation described in Vincent (2014), with the code available at www.comet-toolbox.com.

At first, the Finson–Probstein analysis shows that dust emitted continuously from the asteroids in the last three months of 2018 would lead to a broad tail encompassing both tails 1 and 2. In order to reproduce the observations, we need to consider several discrete events. Each event creates one tail, and the width of each tail informs us about the duration of the dust release.

By fitting tail width/orientation over the full dataset, we get consistent constraints that can explain all the observations. Our analysis shows that dust was emitted during two separate events:

- Tail 1 (the longer) was created over a period of two weeks, from 2018-10-25 to 2018-11-9.
- Tail 2 (the shorter) was created over a period of 10 d, from 2018-12-29 to 2019-1-8.

Table 2. Position of tails in the active asteroid 6478 Gault.

Date (UT)	r_b^* (au)	Δ^* (au)	PsAng* ($^\circ$)	PsAMV* ($^\circ$)	Tail 1	Tail 2
January 8.75	2.468	1.853	303.4	269.7	~292	
January 12.83	2.461	1.799	305.2	269.9	~292	
January 17.87	2.451	1.737	307.5	270.1	~293	
January 25.75	2.435	1.645	312.1	270.7	~293	
February 7.83	2.409	1.518	323.5	271.7	~295	~310
March 1.58	2.364	1.396	21.4	272.7	~292	~307
March 26.58	2.310	1.416	92.6	271.1	~267	~90
April 6.67	2.285	1.473	101.0	269.5	~243	~150

* r_b and Δ are the geocentric and heliocentric distances in au. PsAng is the position of the extended Sun–comet vector, measured from north toward east. PsAMV is the negative of the target’s heliocentric velocity vector, measured from north toward east.

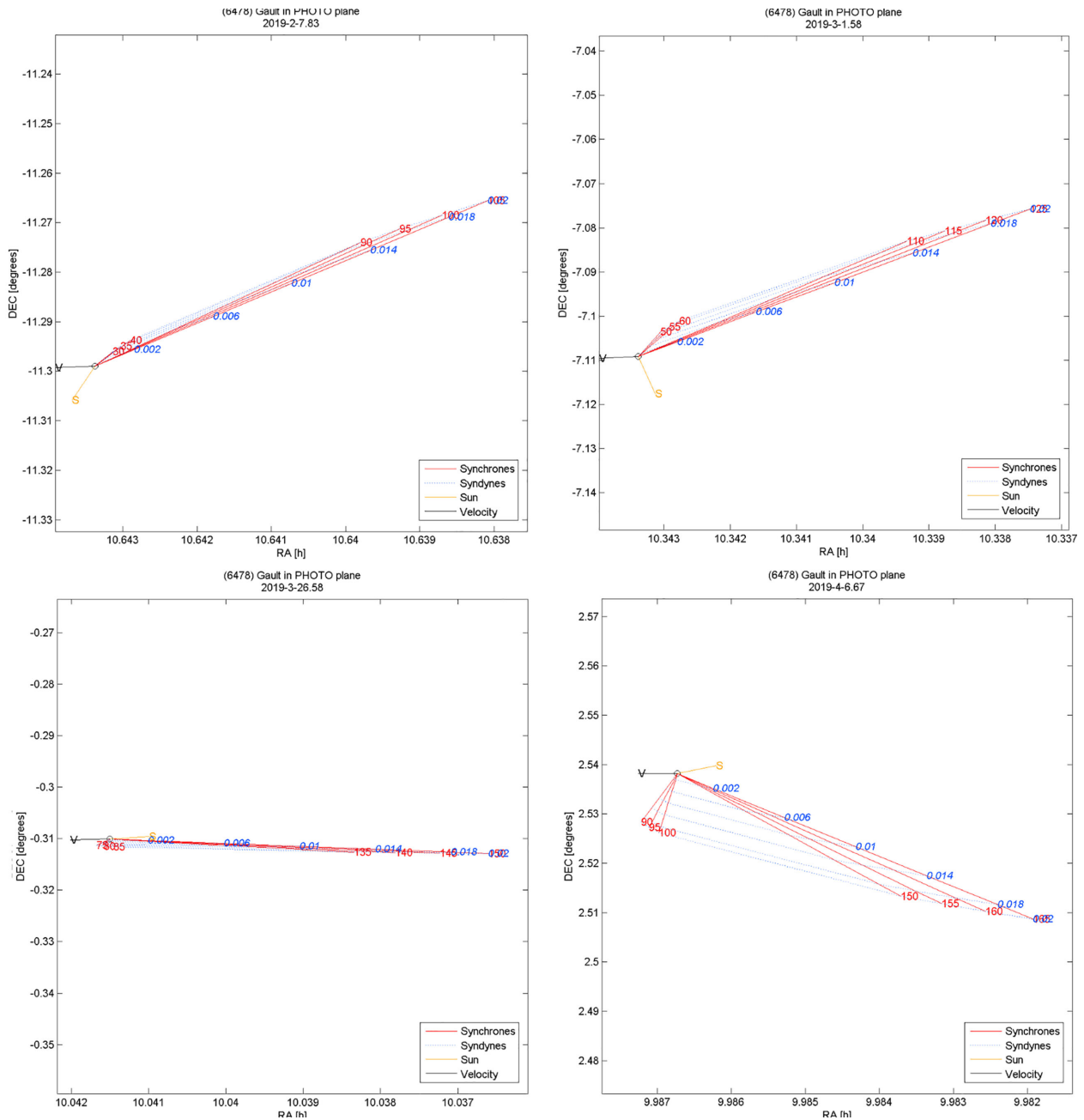
**Fig. 8.** Best-fitting Finson–Probstein diagrams for dates showing both tails (see figure 1). (Color online)

Figure 8 shows the best-fitting Finson–Probstein diagrams for dates showing both tails. Our model can reproduce both tails, and is consistent with the results published by Hui, Kim, and Gao (2019).

Tail 1 always extends beyond the borders of our images, and we cannot accurately constrain the size of its grains. However, tail 2 is finite in our dataset and extends to at most 0.4 arcmin from the asteroid. Beyond that, the tail photometric signal cannot be distinguished from the image background. This puts a strong upper limit on the beta ratio of the particles, which describes their sensitivity to the radiation pressure and is a function of their size: above $0.1\ \mu\text{m}$, smaller particles are more easily swept away than larger ones.

From the extent of tail 2, and within the limits of the instrument sensitivity at the edge of the tail, we derive a maximum beta value of 0.02, which for typical material would indicate a grain size larger than $20\ \mu\text{m}$ (Burns et al. 1979). This falls within the range determined by Hui, Kim, and Gao (2019).

Our model assumes that dust grains leave the nucleus with zero relative velocity. It is possible that larger grains were also emitted with some velocity above the escape speed of Gault, but this cannot be constrained from our observations.

5 Summary

We acquired photometric and spectroscopic observations on 37 nights from 2019 January to April using several telescopes, LOT (1 m telescope) and SLT (40 cm telescope) at Lulin Observatory, and the 2.4 m telescope at Lijiang station of Yunnan Observatory. The results are summarized as follows:

- (i) The low amplitude of our lightcurve data cannot confirm the rotation period of ~ 2 hr (Kleyna et al. 2019) or ~ 3.36 hr (Ferrín et al. 2019) for Gault. These results are compatible with an asteroid observed pole-on or an object having a spherical shape, akin to asteroid Ryugu and Bennu, or low-level cometary activity at the time of observation.
- (ii) Through comparing the known relative reflectance (i.e., the Bus–DeMeo system) and average colors ($B - V_{\text{avg}} = 0.764 \pm 0.045$, $V - R_{\text{avg}} = 0.450 \pm 0.023$), Gault can be classified as a Q-type asteroid.
- (iii) By comparing the spectrum of Gault with known classes defined by the Bus–DeMeo taxonomy, we confirmed that our spectrum is very similar to Q-type asteroids. As a result of photometric and spectroscopic measurements, Gault’s physical properties is closer to

the Phocaea collisional family instead of the Tamara family.

- (iv) By using Finson–Probstein analysis, the grain size for tail 2 is larger than $20\ \mu\text{m}$. Unfortunately, we cannot accurately constrain the size of tail 1’s grains due to the limitation of the FOV.

Acknowledgments

We particularly acknowledge the staffs of the Lijiang 2.4 m telescope and the Lulin 1.0 m telescope for providing assistance with our observations. This publication has made use of data collected at Lulin Observatory, partly supported by MOST grant 108-2112-M-008-001. This work was supported by MOST 105-2112-M-008-002-MY3, MOST 107-2119-M-008-012, and MOST 108-2112-M-008-004 from the Ministry of Science and Technology of Taiwan. Analysis of the project also funded by the National Science Foundation of China (NSFC, No. U1731122).

References

- Agarwal, J., Jewitt, D., Weaver, H., Mutchler, M., & Larson, S. 2016, *CBET*, 4306, 1
- Bevington, P. R., & Robinson, D. K. 1992, *Data Reduction and Error Analysis for the Physical Sciences* (New York McGraw-Hill)
- Bodewits, D., Kelley, M. S., Li, J.-Y., Landsman, W. B., Besse, S., & A’Hearn, M. F. 2011, *ApJ*, 733, L3
- Burns, J. A., Lamy, P. L., & Soter, S. 1979, *Icarus*, 40, 1
- Bus, S. J., & Binzel, R. P. 2002, *Icarus*, 158, 146
- Chandler, C. O., Kueny, J., Gustafsson, A., Trujillo, C. A., Robinson, T. D., & Trilling, D. E. 2019, *ApJ*, 877, L12
- Dandy, C. L., Fitzsimmons, A., & Collander-Brown, S. J. 2003, *Icarus*, 163, 363
- DeMeo, F. E., Binzel, R. P., Slivan, S. M., & Bus, S. J. 2009, *Icarus*, 202, 160
- Elst, E. W., Pizarro, O., Pollas, C., Ticha, J., Tichy, M., Moravec, Z., Offutt, W., & Marsden, B. G. 1996, *IAU Circ.*, 6456, 1
- Ferrín, I., Fornari, C., & Acosta, A. 2019, *MNRAS*, 490, 219
- Finson, M. L., & Probstein, R. F. 1968, *ApJ*, 154, 353
- Hale, A., Berry, R., & Weiland, H. 2019a, *CBET*, 4594, 2
- Hale, A., Weiland, H., & Berry, R. 2019b, *CBET*, 4597, 1
- Howell, E. S. 1995, PhD thesis, University of Arizona
- Hsieh, H. H., et al. 2012a, *AJ*, 143, 104
- Hsieh, H. H., et al. 2012b, *ApJ*, 748, L15
- Hsieh, H. H., et al. 2015, *ApJ*, 800, L16
- Hsieh, H. H., et al. 2018a, *AJ*, 156, 223
- Hsieh, H. H., & Chavez, J. 2017, *CBET*, 4388, 1
- Hsieh, H. H., Ishiguro, M., Knight, M. M., Micheli, M., Moskovitz, N. A., Sheppard, S. S., & Trujillo, C. A. 2018b, *AJ*, 156, 39
- Hsieh, H. H., Jewitt, D. C., & Fernández, Y. R. 2004, *AJ*, 127, 2997
- Hsieh, H. H., Jewitt, D., & Ishiguro, M. 2009, *AJ*, 137, 157
- Hsieh, H. H., Jewitt, D., Lacerda, P., Lowry, S. C., & Snodgrass, C. 2010, *MNRAS*, 403, 363
- Hsieh, H. H., Meech, K. J., & Pittichová, J. 2011, *ApJ*, 736, L18
- Hsieh, H. H., & Sheppard, S. S. 2015, *MNRAS*, 454, L81
- Hui, M.-T., & Jewitt, D. 2015, *AJ*, 149, 134

- Hui, M.-T., Kim, Y., & Gao, X. 2019, MNRAS, 488, L143
Jehin, E., Ferrais, M., & Moulane, Y. 2019, CBET, 4606, 1
Jewitt, D. 2015, AJ, 150, 201
Jewitt, D., Agarwal, J., Weaver, H., Mutchler, M., & Larson, S. 2013, ApJ, 778, L21
Jewitt, D., Kim, Y., Luu, J., Rajagopal, J., Kotulla, R., Ridgway, S., & Liu, W. 2019, ApJ, 876, L19
Jewitt, D., Yang, B., & Haghighipour, N. 2009, AJ, 137, 4313
Kleyna, J. T., et al. 2019, ApJ, 874, L20
Landolt, A. 1992, AJ, 104, 340
Lee, C.-H. 2019a, Astronomer's Telegram, 12468, 1
Lee, C.-H. 2019b, AJ, 158, 92
Lomb, N. R. 1976, Ap&SS, 39, 447
Marsset, M., et al. 2019, ApJ, 882, L2
Moreno, F., et al. 2011, ApJ, 738, 130
Moreno, F., et al. 2019, A&A, 624, L14
Popescu, M., Birlan, M., & Nedelcu, D. A. 2012, A&A, 544, A130
Pravec, P., & Harris, A. W. 2000, Icarus, 148, 12
Sanchez, J. A., Reddy, V., Thirouin, A., Wright, E. L., Linder, T. R., Kareta, T., & Sharkey, B. 2019, ApJ, 881, L6
Smith, K. W., Denneau, L., Vincent, J.-B., & Weryk, R. 2019, CBET, 4594, 1
Tonry, J. L., et al. 2018, PASP, 130, 064505
Vincent, J. 2014, in Asteroids, Comets, Meteors 2014, ed. K. Muinonen et al. (New York: Association for Computing Machinery), 565
Wang, C.-J., et al. 2019, Res. Astron. Astrophys., 19, 149
Ye, Q., et al. 2019a, ApJ, 874, L16
Ye, Q., Kelley, M. S. P., Bodewits, D., Bolin, B., Chang, C.-K., & Lin, Z.-Y. 2019b, Astronomer's Telegram, 12450, 1